



Differential interference contrast microscopy with adjustable plastic Sanderson prisms

SONIKA RATHI, NICHOLAS ZOUBEK, VIVIAN J. ZAGARESE, AND DANIEL S. JOHNSON* 

Department of Physics and Astronomy, Hofstra University, Hempstead, New York 11549, USA

*Corresponding author: Daniel.S.Johnson@Hofstra.edu

Received 22 October 2019; revised 23 December 2019; accepted 20 February 2020; posted 6 March 2020 (Doc. ID 381056); published 7 April 2020

Differential interference contrast (DIC) microscopy is a technique to image spatially dependent gradients in optical path lengths. Contrast is produced through the splitting of polarized light with quartz Wollaston prisms. Here we demonstrate that light splitting for DIC microscopy can also be achieved with Sanderson prisms consisting of polycarbonate bars under a bending load. Comparable image contrast while imaging cultured cells was achieved with this alternative technique. These results demonstrate an inexpensive and easily adjustable alternative to traditional quartz Wollaston prisms. © 2020 Optical Society of America

<https://doi.org/10.1364/AO.381056>

1. INTRODUCTION

Differential interference contrast (DIC) microscopy is a transmitted light imaging technique initially developed in the 1950s [1–4]. The emphasis of the technique is the creation of image contrast between neighboring (~ 100 – 1000 nm) sample regions based on differences in optical path length (OPL). OPL depends on the refractive index and thickness of the sample through which light passes, and thus contrast in DIC represents spatial gradients in the sample refractive index.

DIC microscopy is used to image OPL gradients in a variety of samples including live cells, thin sections of biological tissues, microtubules, minerals, and semiconductors [5–7]. For example, this technique can be used to visualize the boundary between a cell's nucleus and cytoplasm (the nuclear envelope) since light passing just inside the envelope (in the nucleus) experiences a different OPL than the light passing just outside the envelope (in the cytoplasm). In this scenario, the two paths usually have different OPLs because the refractive index is typically lower in the nucleus than the cytoplasm [8,9]. This difference is represented as intensity contrast in the DIC image.

Analysis of OPL gradients in DIC microscopy occurs through an interferometry technique. The illumination light is split, based on polarization, into two spatially separated paths with a Wollaston prism located one focal length prior to a condenser lens [10]. This separation is typically on the order of $1\ \mu\text{m}$, and the paths are distinguished from each other by being orthogonally polarized. These polarized states are initially formed with a linear polarizer at 45° relative to the plane that contains the split paths. Prior to splitting, the light is coherent at any given position, though it does not need to be coherent across the whole beam. After splitting, the relative phase between orthogonal

components that originate from a specific initial beam position is conserved. As a split pair travels through the sample, a relative phase shift is introduced if there is a refractive-index-dependent OPL difference along the two paths [10]. After the light passes through the sample, another prism located one focal length after the objective recombines the split light paths. The recombined beams form an elliptically polarized state, which is analyzed with a second polarizer (“analyzer”). Typically, the analyzer is oriented 90° relative to the first polarizer (crossed polarized). If there is no difference in OPL between the two paths, then the recombined light has the same initial polarization. This results in maximum extinction by the crossed polarizer and creates a dark image. However, if there is a half-wavelength OPL difference between the paths, then the recombined light has a polarization that is rotated 90° from the initial state prior to the first prism. This scenario results in maximum transmission by the crossed polarizer, forming a bright image. With crossed polarizers, regions with no variation in refractive index appear dark, and the boundaries between regions of different refractive indices appear bright. A biological example of a bright region, with a gradient in refractive index, is the boundary between the nucleus and the cytoplasm.

Wollaston (or similar Nomarski) prisms are typically used for splitting and recombining the light in DIC microscopy. These prisms consist of two triangular birefringent quartz wedges cemented together with their fast axes each in a different orientation. Illumination light polarized at 45° relative to the prism effectively creates two orthogonal linear polarization states that are either parallel or perpendicular to the Wollaston orientation [10]. The light in each polarization state experiences a different refractive index when traveling through the

first versus the second quartz element of the prism, and at the transition between the two elements each polarization component is refracted in a different direction. Placing a prism one focal length before the condenser and one focal length after the objective results in the split and recombined light being parallel while passing through the sample.

The divergence angle of Wollaston prisms for DIC imaging is typically on the order of $\sim 100 \mu\text{rad}$ [11], which is achieved with precision-cut quartz with shallow wedge angles. Manufacturing the large crystal prisms is expensive (thousands of USD), and there is no capability of modifying the divergence angle without using different prisms. Sanderson devised an alternative Wollaston-like prism that uses inexpensive stressed photoelastic bars (less than 1 USD) instead of quartz-based prisms [12]. This prism was demonstrated for use in a Schlieren interferometer [13]. Here we demonstrate the use of a Sanderson prism for DIC microscopy.

2. SANDERSON PRISM

Sanderson and colleagues quantitatively predicted split angles for orthogonal polarizations of light passing through a clear photoelastic prismatic bar under applied stress [13]. In this model, the two ends of the bar undergo an applied bending moment in opposite directions, resulting in a tensile/compressive stress gradient in the central region of the bar (Fig. 1). In a photoelastic material, this stress gradient results in a refractive index gradient, which will deflect normal incident light [like a gradient-index (GRIN) lens refracting light]. Furthermore, the refractive index gradient is polarization dependent, with the refractive index increasing for one principle polarization (for example, parallel to the bar centerline), while decreasing for the other principle polarization (perpendicular to the centerline). Thus, the two polarizations of light passing through the bar are split after passing through the bar.

The polarization-dependent refractive index gradient of a stressed bar mimics the gradient in a Wollaston prism. Therefore, orthogonal polarizations of light angularly diverge after passing through the stressed bar. To replace quartz prisms

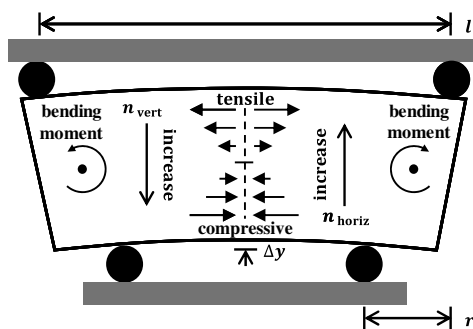


Fig. 1. Illustration of a stressed photoelastic bar. Pins on rods above and below the bar generate a bending moment near the ends of the bar, resulting in a vertical stress gradient in the middle of the bar. Above the horizontal centerline the bar is stretched, while below the centerline the bar is compressed. The stress gradient generates a polarization-dependent refractive index gradient. This refractive index gradient results in horizontally polarized light (incident normal on the bar) to be deflected upward while vertically polarized light is deflected downward.

with Sanderson prisms in DIC microscopy, we designed stressor frames (Fig. 2) to be incorporated into an inverted microscope (Olympus IX-81). For the objective side prism, we used an open frame system [12] where force was applied evenly to each side of the plastic through a loading bar attached to a single screw [Fig. 2(a)]. The condenser side loading frame was designed to match the size of the Wollaston mount in the Olympus condenser housing, and stress was applied to each side of the bar with two set screws [Fig. 2(b)]. 3/32-in. thick clear polycarbonate bars were used for these frames (McMaster-Carr). Both frames were fabricated with a 3D printer (Ultimaker 2+) out of polyactic acid plastic.

To verify the prism diverged orthogonal polarizations of light, we measured the deflection of normally incident 488 nm laser light (Omnichrome 543-AP-A01) after passing through the prism. Prior to the prism, a vertical or horizontal polarization state, relative to the open frame illustrated in Fig. 1, was created with a half-wave plate (Thorlabs AHWP05M-600). After the prism, the beam deflection was measured at a distance of 2.2 m with a lateral effect position detector (Thorlabs PDP90A). The divergence angle between horizontal and vertical polarization was determined from the difference in positional beam deflection divided by the detector distance. With this measurement, we verified the prism diverged orthogonal polarizations of light and that the divergence angle depended linearly on the amount the bar was bent [Fig. 3(a)]. These observations follow previous predictions [13], where the paraxial divergence angle ϵ depends linearly on the bar deflection Δy :

$$\epsilon = \frac{\lambda E}{f_\sigma} \frac{24b}{4r^2 - 3l^2} \Delta y,$$

where $\frac{\lambda E}{f_\sigma} = 0.193$ for polycarbonate [13], b is the thickness of the bar, and r and l are the loading point positions (see Fig. 1). In this prediction, the divergence angle is independent of wavelength. Note that Fig. 3(a) is in terms of loading screw displacement, which scales approximately linearly relative to bar deflection.

To incorporate the Sanderson prism into a DIC microscope, we adjusted the divergence angle to be approximately 95% of the Wollaston prism (Olympus U-DICTS; a Nomarski prism, described below): $\sim 65 \mu\text{rad}$ and $\sim 69 \mu\text{rad}$, respectively. The small difference was to compensate for demagnification when the Sanderson prism was positioned at an image of the objective's back focal plane (BFP; see below). In addition, when the Sanderson and Nomarski prisms were observed between crossed linear polarizers, there were roughly similar wavelength-dependent interference bands [Fig. 3(b)]. For this measurement, the polarizers were placed 45° relative to gradient direction [in Fig. 3(b) one polarizer was 45° towards the top left and the other 45° to the bottom left] and were illuminated with a broad-spectrum lightbox. At any given position on the prism, the initial horizontal and vertical polarization of light were in phase. However, as the light passed through the prism, a relative phase was introduced between the orthogonal polarizations, generating an elliptically polarized state that was then analyzed with the second polarizer. In regions where there was no relative phase shift, the light was extinguished by the second polarizer (dark 90° vertical center line). In regions where there was a

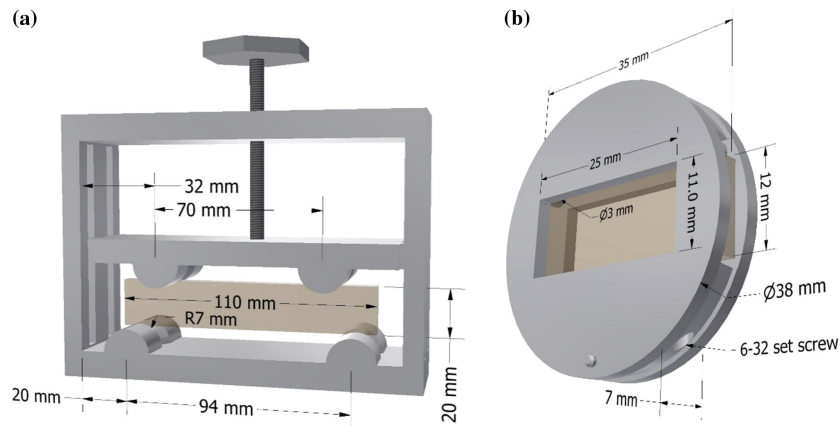


Fig. 2. Illustration of (a) open frame and (b) condenser frame used to apply stress to clear polycarbonate bars. For the open frame the bending moment was modulated by adjusting the number of turns in the central screw; for the condenser frame, the bending moment was modulated by adjusting the number of turns in two set screws.

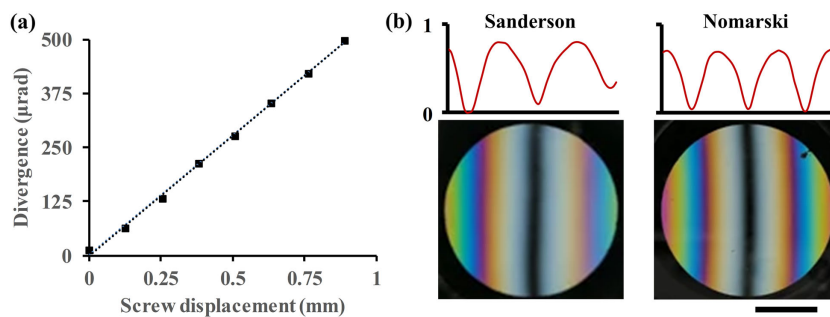


Fig. 3. Polarization-dependent refractive index gradient was created in a stressed plastic bar with an open frame. (a) As bending of polycarbonate bar increased, as indicated by frame screw displacement, the divergence of orthogonal polarizations of light increased linearly. (b) As indicated by interference patterns when prisms were observed between crossed polarizers, the two prisms had roughly the same polarization-dependent refractive index gradient when configured for imaging. Line plots are transmittance intensity profiles of the red color (taken from the RGB color photo) along a horizontal line through the image (averaged with a line width of 15 pixels). The profiles were normalized to the red illumination intensity. The fringe pattern was nonsymmetric for the Sanderson prism, with a higher transmittance on the right side of the prism (compressed side) compared to the left side (stretched side). Scale bar: 10 mm.

phase shift, there were bright, wavelength-dependent bands. For example, blue light has a shorter wavelength than red and therefore required less wavefront delay to achieve a 90° phase shift. This difference resulted in blue appearing next to the dark central band. This blue band was then followed by a white band (a mixture of colors), a yellow band, and finally a red band. This color pattern is similar to the color bands observed with thin-film interference or Newton's rings [14].

The colors in the interference pattern, particularly on the right side of the prism, were less defined for the Sanderson prism as compared to the Nomarski prism. This is illustrated by a horizontal line profile of the transmittance of the red light [Fig. 3(b)]. For the Sanderson prism the dark central band had a transmittance of 10%, while the Nomarski prism had a transmittance of 4%. The first maximum intensity bands on either side of the center had transmittances of approximately 70% and 80% for the Nomarski and the Sanderson prisms, respectively. The next dark bands were nonsymmetrical for the Sanderson prism, with a transmittance of 27% on the right side and 0% on the left. The dark bands were 3% for the Nomarski prism. The higher transmittance for the Sanderson prism may have

indicated that the prism introduced ellipticity, which could have degraded the ability to optically distinguish the two split beams during DIC imaging. The asymmetric and higher transmittance may have been caused by bending of the bar in an unintended direction, like twisting along the long axis. Alternatively, there may have been nonlinear properties of the stressed plastic that introduced unexpected aberrations.

3. DIC IMAGING

As described above, in DIC microscopy, quartz Wollaston prisms are positioned so that their divergence and convergence locations are one focal length before the condenser lens and after the objective lens. However, with high-magnification objectives, with short focal lengths, the BFP is typically within the objective, and therefore it is not possible to place a Wollaston prism at this position. Instead, a modified Wollaston-like prism, a Nomarski prism, is used [2,4]. This prism has its convergence point outside the prism and is placed so that this convergence point is at the objective BFP [Fig. 4(a)]. To facilitate placing the Sanderson prism at the BFP, we added a 200 mm lens (Lens 1,

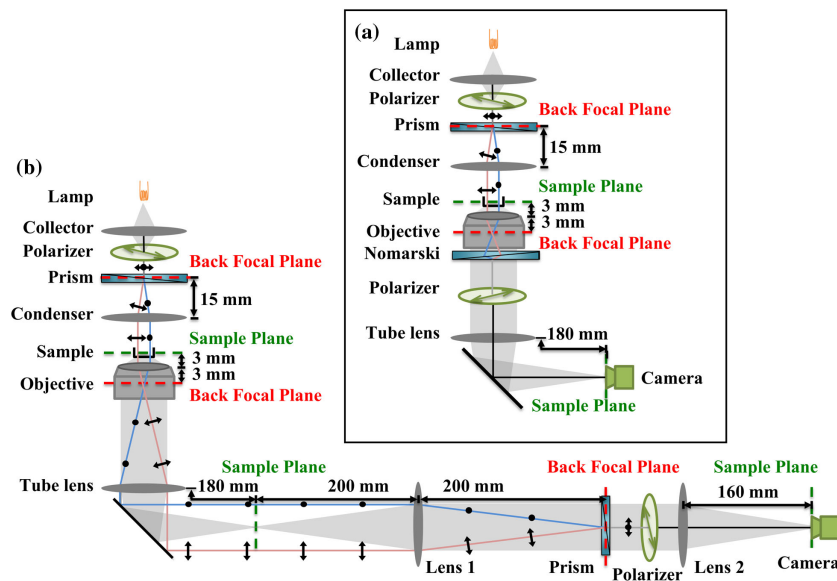


Fig. 4. Illustrations of imaging optics. (a) Typical DIC configuration with a Nomarski prism after the objective, aligned with the BFP convergence point. The split red and blue lines represent polarizations parallel and perpendicular to the page, respectively. (b) An objective-side Sanderson prism is placed at an image of the BFP created by the tube lens and lens 1. Lens 2 creates a second image of the sample plane for imaging with a camera.

Newport PAC064AR.14) to the system to create an image of the BFP beyond the objective [Fig. 4(b)]. Additionally, a second 160 mm lens (Lens 2, Qioptic G322267000) was added to create a second image of the sample plane. Samples were imaged with a 60X objective (Olympus UPLAPO60XW 1.2NA) and captured with a digital CCD camera (Hamamatsu ORCA-ER).

With the Sanderson prism at the imaged BFP, we acquired DIC images of live HeLa cells plated in glass bottom dishes (MakTek P35G-0.170-14-C). These images had a characteristic ‘3D’ shadow appearance [Fig. 5(b)], which is typical for DIC imaging. The contrast was similar to the same image acquired with a quartz Nomarski prism [Fig. 5(a)], though qualitatively the image resolution appeared to be a little better with the quartz prism. Quantitatively, the radial average of a 2D power spectrum (using FFT and Radial Profile Plot in ImageJ [15]) [Fig. 5(e)] revealed that the quartz prism had more power at higher spatial frequencies, indicating greater image contrast. The spatial cutoff frequency between low-frequency image signal and high-frequency noise was also greater for the quartz prism, indicating its image had higher spatial resolution.

Next, we imaged the same cells with a Sanderson prism replacement for the Wollaston condenser [Fig. 2(b)]. Like the objective-side prism, we first configured the load on the ends of the polycarbonate by matching the beam divergence and refractive index profile to the microscope’s Wollaston condenser (Olympus IX-DPO60). Here the divergence was $\sim 14 \mu\text{rad}$. As with the objective-side Sanderson prism, we observed similar but slightly better contrast with the quartz prism [Figs. 5(a), 5(c), 5(e)]. Finally, we imaged cells with both objective- and condenser-side Sanderson prisms, and we observed slightly better contrast and resolution with the quartz prisms [Figs. 5(a), 5(d), 5(e)]. In all these scenarios, the image quality was qualitatively observed to be marginally better with the quartz prisms. The lower quality with the Sanderson prism is possibly related to

the optical aberrations observed when the prism was visualized with the crossed polarizers [Fig. 4(b)].

Unlike the quartz Wollaston-like prisms, the divergence angle and thus the parallel ray separation could be adjusted with the Sanderson prism. When we modified the bending moment on the objective-side Sanderson prism, by adjusting the number of turns in the loading screw [Fig. 2(a)], there was a clear qualitative change in the image contrast [Figs. 6(a)–(d)]. Quantitatively, the image contrast, as indicated by the power of the spectrum, was also greater, with a larger bending moment on the plastic bar [Fig. 6(e)]. The flexibility to change the bending of the plastic bar made it possible to quickly adjust the system to produce the best image contrast.

Like a quartz-based system, we were also able to add “bias retardation” to the image by translating the objective-side Sanderson prism perpendicular to the optical axis (Fig. 7). In practice this modulation was accomplished by translating the entire open frame on an optical post. This translation shifted the relative phase between the split paths. For example, with zero bias, regions with no refractive index gradient would be extinguished by the objective-side crossed polarizer. This scenario was observed in the background and cell cytoplasm [Fig. 7(b)]. Note that, as is typical with DIC imaging, the two polarizers were configured to be slightly away from 90° to facilitate a small amount of light to pass). When bias was added by translating the prism, the image appeared dark on the lower left edge of the cell and bright on the upper right edge [Fig. 7(a)]. Alternatively, when the prism was translated to the other side of the optical axis, the lower left edge appeared bright and the upper right edge appeared dark [Fig. 7(c)]. Adjusting bias retardation makes it possible to optimize the image contrast in the region of interest.

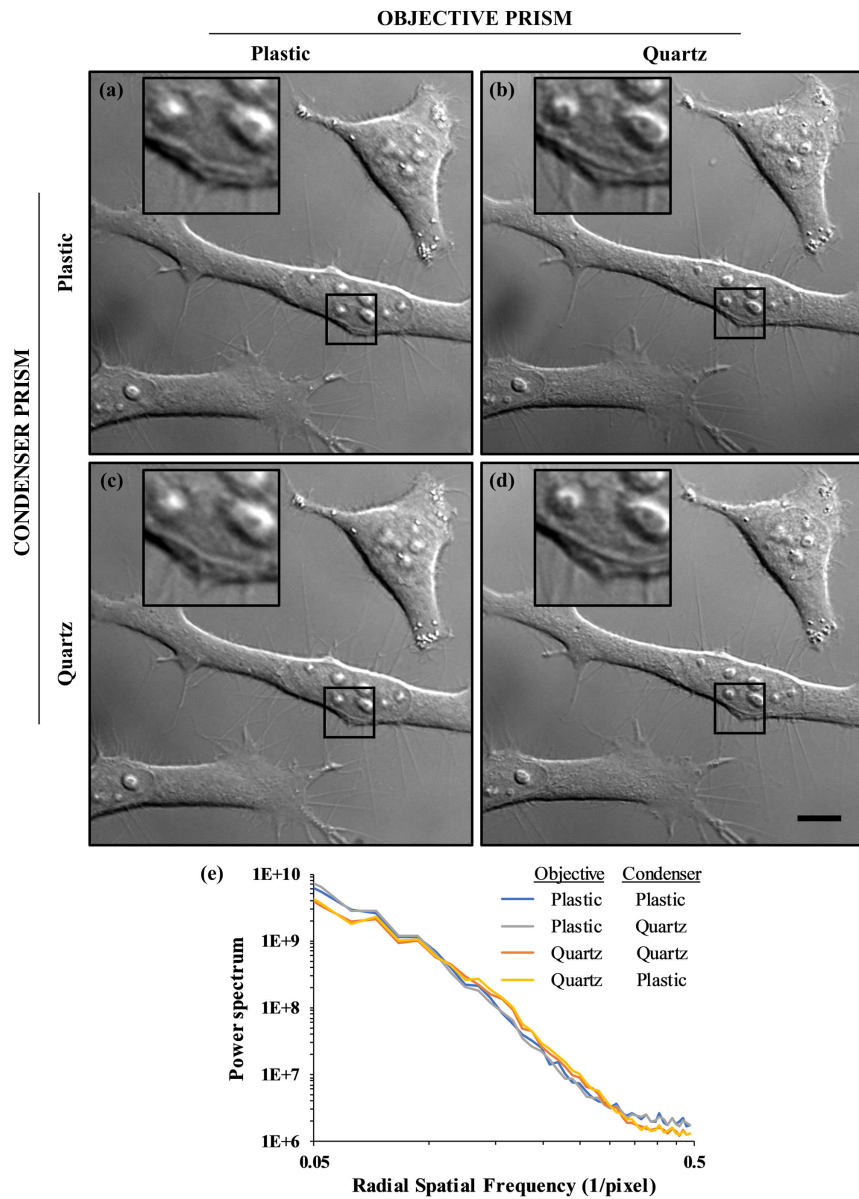


Fig. 5. (a–d) DIC images of cultured HeLa cells with either a quartz Wollaston-like prism or plastic Sanderson prisms in the imaging optics. Image intensity scaled with 0.35% of pixels saturated. The inset is from the black box region. The scale bar represents 10 μm . (e) Radial average profile of the 2D power spectrum from a 128 pixel \times 128 pixel region of the central cell's nucleus.

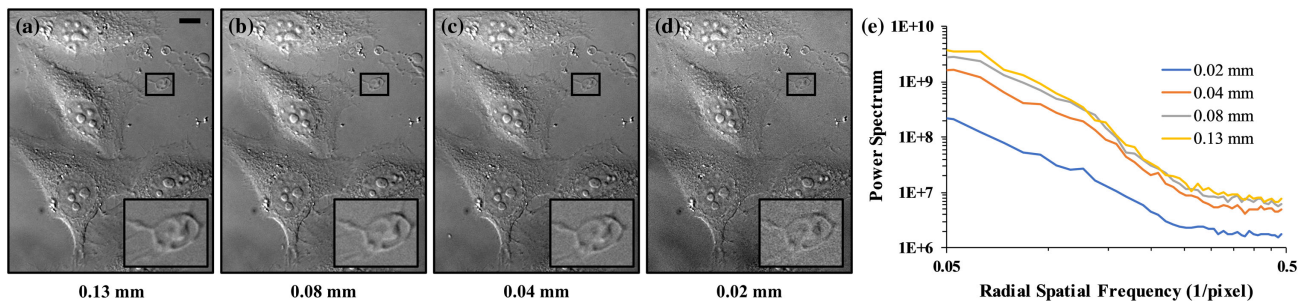


Fig. 6. (a–d) Image contrast affected by the amount of stress on the plastic as indicated by the open frame screw displacement. Image intensity scaled with 0.35% of pixels saturated. The inset is from the black box region. The scale bar represents 10 μm . (e) Radial average profile of the 2D power spectrum of a 128 pixel \times 128 pixel region in the lower left cell's nucleus.

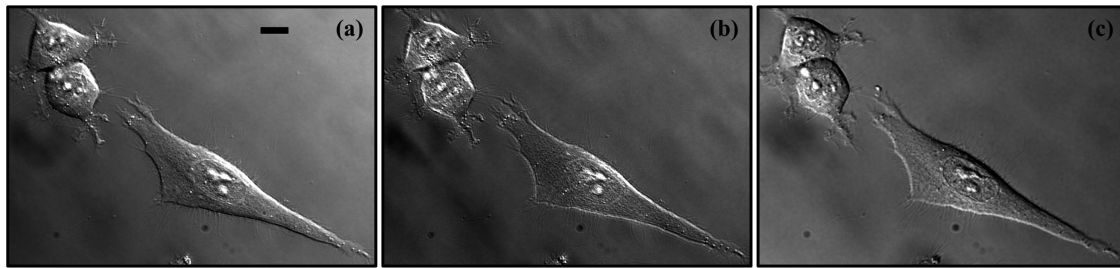


Fig. 7. (a–c) Translating the Sanderson prism perpendicular to the optical axis altered the image bias retardation. Here the dark and bright edges of the cell swapped positions between left and right images. Image intensity scaled with 0.35% of pixels saturated. The scale bar represents 10 μm .

4. CONCLUSION

As shown here, stressed plastic Sanderson prisms function as an alternative to traditional quartz Wollaston prisms for producing DIC images. Unlike conventional DIC systems, where each prism has a fixed divergence angle, this technique enables the development of a fully tunable system, where the divergence angle can be adjusted for any given objective lens or any given condenser, or it can be adjusted to generate the best contrast for any given sample condition. The tunable prism may also be useful for alternative DIC techniques, like PlasDIC. In PlasDIC, a single prism is utilized after the objective, eliminating the cost of one of the prisms. The microscope still produces a similar contrast, though typically with lower resolution.

Currently there are a number of imaging systems being developed for users with limited budgets [16–20]. We envision the incorporation of Sanderson prisms into systems like these, facilitating DIC imaging with a system that has a total cost that is less than the Wollaston prisms themselves. In this system, the components for the prisms were approximately 1 USD, and we imagine a complete system, with optics and image sensor, costing roughly 100 USD. Eliminating the cost of the Wollaston prisms also makes DIC accessible to users who utilize economical imaging techniques, like phase contrast or Hoffman modulation contrast (HMC). HMC produces similar 3D-like images but has lower resolution and detection sensitivity [10].

Since many of these economical systems are targeted to educational environments, we also imagine they will provide an educational platform for providing training in imaging systems, basics of linear and elliptical polarization, phase microscopy, and concepts in photoelasticity. In addition, there has been a proliferation of non-conventional systems, such as miniaturized and lens-less imaging platforms [21–26]. With the physical and economic constraints that come with these systems, we envision creative use of Sanderson prisms may be a viable alternative for incorporating DIC imaging.

A challenge with the adoption of Sanderson prisms for DIC imaging is the placement of a prism in the BFP of the objective. For budget and educational settings, it will likely be possible to incorporate the Sanderson prism into low-magnification objectives, since they have relatively long focal lengths. Unusual objectives, with access to the BFP, would be necessary for higher-magnification systems. Alternatively, and potentially with more benefit, it may be possible to create more sophisticated refractive index gradients that replicate Nomarski prism divergence profiles. Ideally, this type of system would make it

possible to incorporate the prism directly behind a standard high-magnification objective lens, simplifying the transition from a quartz- to plastic-based prism.

FUNDING. Hofstra College of Liberal Arts and Sciences.

Acknowledgment. We thank Sanford Simon from Rockefeller University for comments on the manuscript and for providing cell samples and access to research equipment. We also thank Steve Campolo for assistance with fabrication of frames.

Disclosures. The authors declare no conflicts of interest.

REFERENCES

1. F. H. Smith, "Interference microscope," U.S. patent 2,601,175 (3 August 1948).
2. G. Nomarski, "Interféromètre à polarisation," French patent 1,059,123 (5 May 1952).
3. F. H. Smith, "Microscopic interferometry," *Research* **8**, 385–395 (1955).
4. G. Nomarski, "Microinterféromètre différentiel à ondes polarisées," *J. Phys. Radium* **16**, 9S–11S (1955).
5. M. Pluta, "Nomarski's DIC microscopy: a review," *Proc. SPIE* **1846**, 10–25 (1994).
6. A. Lasslett, "Principles and applications of differential interference contrast light microscopy," *Microsc. Anal.* **20**, S9–S11 (2006).
7. M. Yenjerla, M. Lopus, and L. Wilson, "Analysis of dynamic instability of steady-state microtubules in vitro by video-enhanced differential interference contrast microscopy with an appendix by Emin Oroudjev," *Meth. Cell Biol.* **95**, 189–206 (2010).
8. M. Schürmann, J. Scholze, P. Müller, J. Guck, and C. J. Chan, "Cell nuclei have lower refractive index and mass density than cytoplasm," *J. Biophoton.* **9**, 1068–1076 (2016).
9. Z. A. Steelman, W. J. Eldridge, J. B. Weintraub, and A. Wax, "Is the nuclear refractive index lower than cytoplasm? Validation of phase measurements and implications for light scattering technologies," *J. Biophoton.* **10**, 1714–1722 (2017).
10. D. B. Murphy and M. W. Davidson, *Fundamental of Light Microscopy and Electronic Imaging*, 2nd ed. (Wiley, 2013).
11. M. Shribak, "Differential Interference Contrast Microscopy (DIC)" in *Biomedical Optical Phase Microscopy and Nanoscopy*, N. T. Shaked, Z. Zalevsky, and L. L. Satterwhite, eds. (Academic, 2013), pp. 19–42.
12. S. R. Sanderson, "Simple, adjustable beam splitting element for differential interferometers based on photoelastic birefringence of a prismatic bar," *Rev. Sci. Instrum.* **76**, 113703 (2005).
13. M. M. Biss, G. S. Settles, M. E. Staymates, and S. R. Sanderson, "Differential Schlieren-interferometry with a simple adjustable Wollaston-like prism," *Appl. Opt.* **47**, 328–335 (2008).
14. E. Hecht, "Interference," in *Optics*, 5th ed. (Pearson, 2017), pp. 390–448.

15. J. Schindelin, I. Arganda-Carreras, E. Frise, V. Kaynig, M. Longair, T. Pietzsch, S. Preibisch, C. Rueden, S. Saalfeld, B. Schmid, and J. Y. Tinevez, "Fiji: an open-source platform for biological-image analysis," *Nat. Methods* **9**, 676–682 (2012).
16. N. A. Switz, M. V. D'Ambrosio, and D. A. Fletcher, "Low-cost mobile phone microscopy with a reversed mobile phone camera lens," *PLoS ONE* **9**, e95330 (2014).
17. A. Skandarajah, C. D. Reber, N. A. Switz, and D. A. Fletcher, "Quantitative imaging with a mobile phone microscope," *PLoS ONE* **9**, e96906 (2014).
18. J. P. Sharkey, D. C. W. Foo, A. Kabla, J. J. Baumberg, and R. W. Bowman, "A one-piece 3D printed flexure translation stage for open-source microscopy," *Rev. Sci. Instrum.* **87**, 025104 (2016).
19. A. Maia Chagas, L. L. Prieto-Godino, A. B. Arrenberg, and T. Baden, "The € 100 lab: a 3D-printable open-source platform for fluorescence microscopy, optogenetics, and accurate temperature control during behaviour of zebrafish, *Drosophila*, and *Caenorhabditis elegans*," *PLoS Biol.* **15**, e2002702 (2017).
20. T. Aidukas, R. Eckert, A. R. Harvey, L. Waller, and P. C. Konda, "Low-cost, sub-micron resolution, wide-field computational microscopy using opensource hardware," *Sci. Rep.* **9**, 7457 (2019).
21. K. K. Ghosh, L. D. Burns, E. D. Cocker, A. Nimmerjahn, Y. Ziv, A. E. Gamal, and M. J. Schnitzer, "Miniaturized integration of a fluorescence microscope," *Nat. Methods* **8**, 871–878 (2011).
22. M. A. Al-Rawhani, J. Beeley, and D. R. S. Cumming, "Wireless fluorescence capsule for endoscopy using single photon-based detection," *Sci. Rep.* **5**, 18591 (2015).
23. G. Barbera, B. Liang, L. Zhang, Y. Li, and D. T. Lin, "A wireless miniScope for deep brain imaging in freely moving mice," *J. Neurosci. Meth.* **323**, 56–60 (2019).
24. A. Greenbaum, Y. Zhang, A. Feizi, P. L. Chung, W. Luo, S. R. Kandukuri, and A. Ozcan, "Wide-field computational imaging of pathology slides using lens-free on-chip microscopy," *Sci. Transl. Med.* **6**, 267ra175 (2014).
25. S. V. Kesavan, F. Momey, O. Cioni, B. David-Watin, N. Dubrulle, S. Shorte, E. Sulpice, D. Freida, B. Chalmond, J. M. Dinten, X. Gidrol, and C. Allier, "High-throughput monitoring of major cell functions by means of lensfree video microscopy," *Sci. Rep.* **4**, 5942 (2014).
26. J. K. Adams, V. Boominathan, B. W. Avants, D. G. Vercosa, F. Ye, R. G. Baraniuk, J. T. Robinson, and A. Veeraraghavan, "Single-frame 3D fluorescence microscopy with ultraminiature lensless FlatScope," *Sci. Adv.* **3**, e1701548 (2017).